PURPOSE-LED
PUBLISHING™

PAPER

Multiple conformal-contact transfer of large-area crack-free transition metal dichalcogenide stacks

View the article online for updates and enhancements.

2D Materials

PAPER

Multiple conformal-contact transfer of large-area crack-free transition metal dichalcogenide stacks

Yu Fu[1,3] , Yilin Niu[1,3] , Guodong Xue[2,3] , Quanlin Guo[2], Chang Liu[2] , Jiale Chen[1], Hao Hong[2], Can Liu[1,*] and Kaihui Liu[2,*]

[1] Key Laboratory of Quantum State Construction and Manipulation (Ministry of Education), Department of Physics, Renmin University of China, Beijing 100872, People's Republic of China
[2] State Key Laboratory for Mesoscopic Physics, Frontiers Science Center for Nano-optoelectronics, School of Physics, Peking University, Beijing 100871, People's Republic of China
[3] These authors contributed equally to this work.
[*] Authors to whom any correspondence should be addressed.

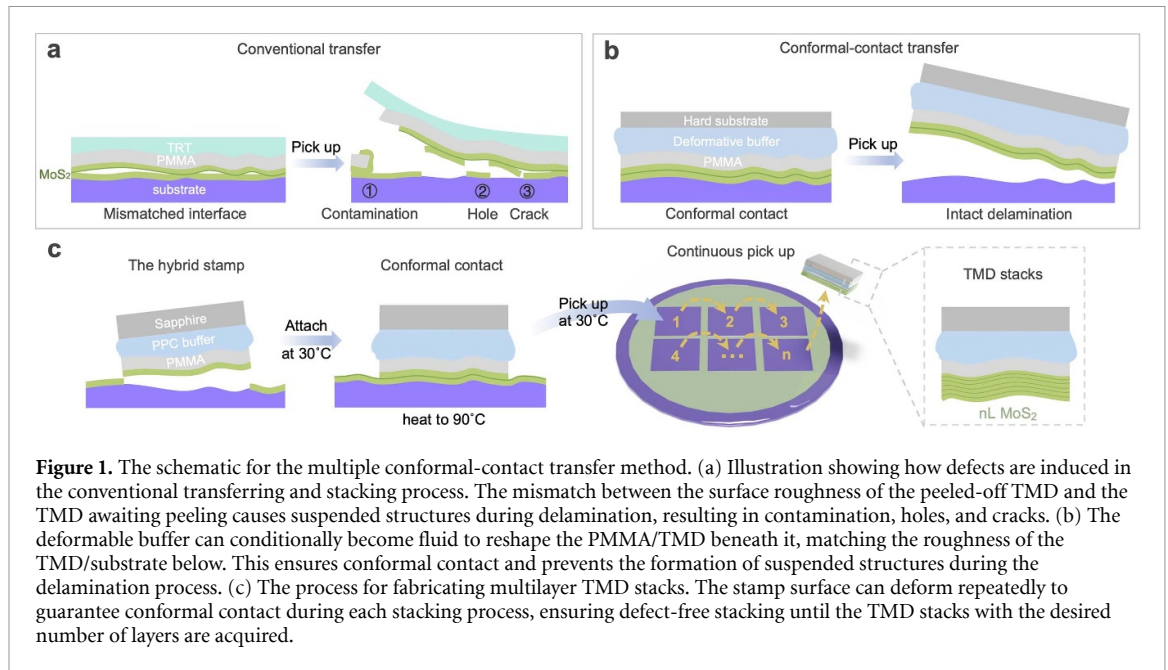E-mail: canliu@ruc.edu.cn and khliu@pku.edu.cn

Abstract

Atomically-thin two-dimensional (2D) transition metal dichalcogenides (TMDs) have emerged as an ideal platform for both physics investigation and device applications. By stacking different layers into homo- or hetero-structures, an extra degree of freedom is involved in further tuning their properties, thereby boosting scenarios in twistronics, moiré photonics and optoelectronics. However, interfacial imperfections such as contaminations and cracks, frequently occur during the layer stacking sequence and accumulate layer by layer, greatly degenerating the interface quality. In this study, we developed a multiple conformal-contact transfer method to construct TMD stacks with crack-free intrinsic interfaces. The design of a deformable buffer layer is crucial to guarantee the conformal contact and intact transfer of each layer, contributing to the successful construction of centimetre-scale TMD stacks up to 8 layers. Precise control over spatial location and interlayer twist angle is also feasibly achieved, evidenced by the stacking-dependent interlayer exciton (IE) effects in WS_2-WSe_2 heterostructures. This work provides a facile and precise approach for architecting 2D stacks with perfect interfaces, which will further accelerate the customized design for their device functionalization.

1. Introduction

Transition metal dichalcogenides (TMDs), distinguished by their sub-nanometer thickness, fast charge transfer, high carrier mobility, and intrinsic spin-valley couplings, have been considered as competitive candidate materials for next-generation electronics, optoelectronics and spintronics [1–4]. Over the last decade, significant advances have been made in the production of TMD films, achieving milestones such as technical route establishment for single crystals and wafer-scale growth from 2 to 12 inches [5–10]. To further facilitate their applications, the development of large-area transfer techniques is crucial [11, 12], especially in the integrations with silicon or incorporation into flexible electronics and deformable optoelectronics [13–15].

Additionally, by piling multiple TMD layers into homo- or hetero-stacks with high-quality interfaces, efficient interfacial charge transfer—a key step for exciton engineering—can be induced, thus broadening their application scenarios in photodetectors, photocatalysts, lasers, and light-emitting diodes [16, 17]. Therefore, a reliable transfer method that ensures consistency both within and across layers during multiple stacking procedure is of vital importance.

Currently, TMD stacks are predominantly fabricated using a cyclic wet-transfer process. This method involves sequentially transferring single-layer TMDs onto a target substrate with the aid of polymers. Each layer is overlaid on top of the previous one, followed by the acetone-washing and annealing to remove the polymers. And this procedure is repeated until the desired layer number is achieved

Figure 1. The schematic for the multiple conformal-contact transfer method. (a) Illustration showing how defects are induced in the conventional transferring and stacking process. The mismatch between the surface roughness of the peeled-off TMD and the TMD awaiting peeling causes suspended structures during delamination, resulting in contamination, holes, and cracks. (b) The deformable buffer can conditionally become fluid to reshape the PMMA/TMD beneath it, matching the roughness of the TMD/substrate below. This ensures conformal contact and prevents the formation of suspended structures during the delamination process. (c) The process for fabricating multilayer TMD stacks. The stamp surface can deform repeatedly to guarantee conformal contact during each stacking process, ensuring defect-free stacking until the TMD stacks with the desired number of layers are acquired.

[18–20]. Nevertheless, impurities are inevitably introduced at the interfaces and progressively accumulate with each added layer, degrading the overall quality of the stacks. Additionally, the repetitive coating-transferring-removing cycle is both time-consuming and labor-intensive, rendering this method impractical for the production of multilayer stacks.

To reduce impurities at the interfaces and enhance stacking efficiency, multiple transfer techniques using an initial TMD layer on polymers to continuously delaminate additional TMD layers have been proposed [21, 22]. Since polymers are only attached to the first layer, the interfaces between TMD layers remain clean during the stacking process. However, it is worth noting that, the polymer's surface roughness can inherit to its attached TMD layers, while layers awaiting delamination followed the substrate's roughness. This roughness mismatch results in gaps between different layers, leading to subsequent formation of suspended structures that introduce defects such as contamination, cracks, and holes in the delamination process [23] (figure 1(a)). These defects accumulate as layer numbers increase, leading to an inhomogeneous layer distribution throughout the stack. Many attempts have been made to achieve conformal contact between the attached interfaces, including incorporating volatile molecules into polymers, or combining polymers with different glass transition temperatures [23, 24], which, however, are disposable and only restricted to monolayer transfer. Therefore, overcoming the roughness mismatch by ensuring conformal contact during every lamination process is crucial to maintaining pristine interface quality in TMD stacks.

Herein, we designed a novel multiple conformal-contact transfer method to achieve crack-free multilayer TMD stacks (figure 1(b)). The core module of

this method is a hybrid stamp featuring a deformable buffer layer that can repeatedly adjust its shape under specific conditions: (i) at high temperatures, the buffer vitrifies into a fluid state, replicating the morphology of layers awaiting delamination on the substrate and inducing conformal contact during each lamination; (ii) at low temperatures, it reverts to a solid state, preventing cracks caused by strains during delamination. This fluid-to-solid state changing cycle ensures that all layers are uniformly and intimately contacted throughout the stacking process.

2. Results

2.1. Multiple conformal-contact transfer of MoS$_2$ stacks

In our design, the hybrid stamp is constructed by pressing a sapphire pre-coated with a thick polypropylene carbonate (PPC) layer into contact with a polymethyl methacrylate (PMMA)-coated MoS$_2$ on SiO$_2$/Si substrate. This assembly was then heated to 150°C, where the PPC became fluid, diffusing beneath the sapphire and achieving conformal contact between the PPC and PMMA/MoS$_2$ interface. Then it was subsequently cooled down to ~30°C to re-solidify the PPC layer. The sapphire/PPC/PMMA/MoS$_2$ stack was then exfoliated in air, creating the hybrid stamp as shown in figure 1(c).

The hybrid stamp, with the initial MoS$_2$ layer attached, was utilized to exfoliate additional MoS$_2$ layers on SiO$_2$/Si substrate. In each stacking cycle, the hybrid stamp was conformally attached to the target MoS$_2$ layer by heating the PPC buffer to its thermoplastic state at 90°C. Note that the sapphire provides robust support, while the PMMA isolates the deformable PPC from tearing the MoS$_2$ layer.
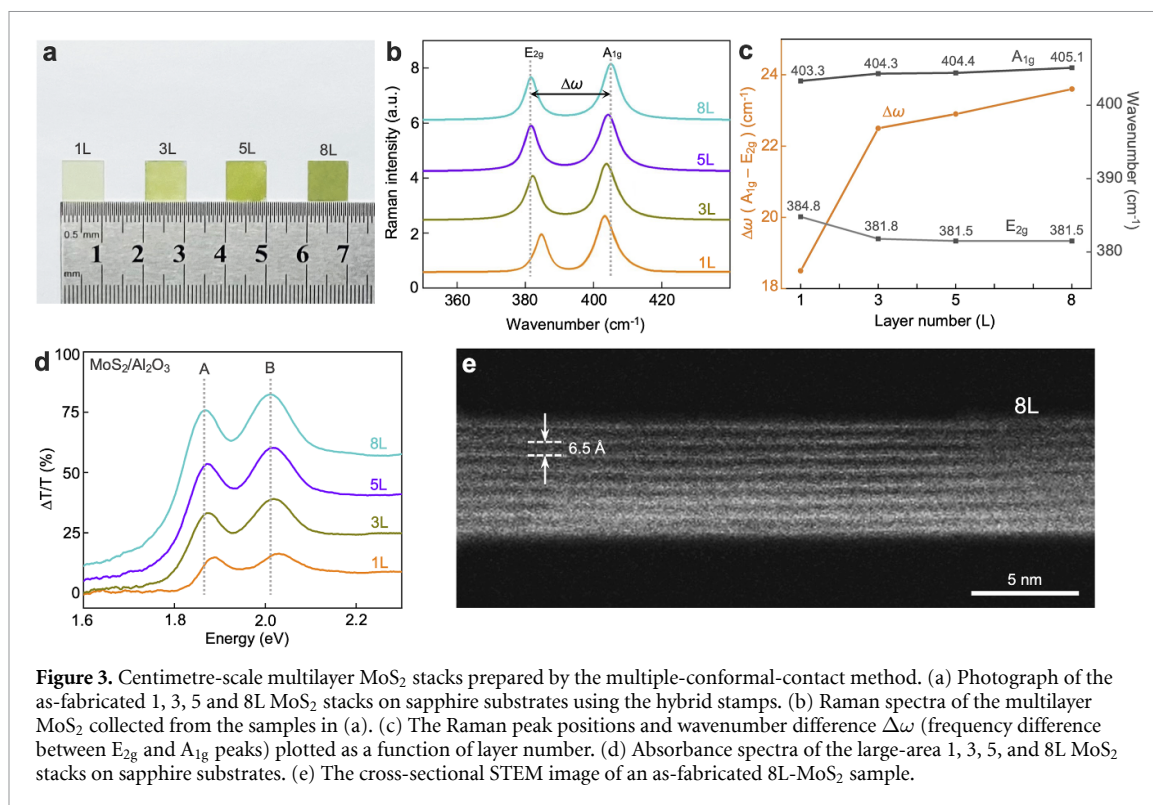
Figure 2. Fabrication of 2L-MoS$_2$ stacks by the multiple conformal-contact method and the comparison with conventional transfer methods. (a), (b) optical images and AFM images of 2L–MoS$_2$ transferred onto SiO$_2$/Si substrates by the hybrid stamp (a$_1$ and b$_1$), PMMA/TRT (a$_2$) and (b$_2$) and PDMS-based (a$_3$) and (b$_3$) methods, respectively. (c), (d) height distributions extracted from the 1L (c) and 2L (d) regions in (b), respectively. (e) Raman mapping of the 2L-MoS$_2$ fabricated by the hybrid stamps based on the intensity of A$_{1g}$ vibration mode.

Delamination of the target MoS$_2$ layer was conducted at ∼30°C, when the PPC returned to a resolidified state. This process was iteratively repeated until the desired number of MoS$_2$ layers was accumulated on the hybrid stamp, with each cycle taking ∼3 min (figure 1(c)). Finally, the polymer layers were removed by acetone washing and annealing, releasing the as-transferred TMD stacks onto target substrates (figure S1). The technique effectively suppressed the appearance of contaminations, cracks, and holes, attributing to the ensured conformal contact between the MoS$_2$ layers. Additionally, it can be applicable to construct other 2D stacks when the adhesion between each component exceeds that between the component and its original substrate.

2.2. Quality confirmation of the as-transferred 2L-MoS$_2$

To demonstrate the effectiveness of our multiple conformal-contact method, a high-roughness SiO$_2$/Si substrate (roughness of ∼4 nm) was intentionally selected as both the growth substrate for MoS$_2$ and the target substrate for transfer. We fabricated three samples of two-layer (2L) MoS$_2$ stacks using

our conformal-contact method, as well as traditional thermal release tape (TRT)/PMMA and polydimethylsiloxane (PDMS) transfer methods for comparative analysis. As shown in figure 2(a)$_1$, an intact film is preserved benefiting from the conformal contact in our method, while pronounced cracks and defects exist on the ones made by TRT/PMMA and PDMS transfer (figure 2(a)$_2$, (a)$_3$).

Atomic force microscope (AFM) images also confirm minimal cracks and contaminations within our stack at the microscopic level (figure 2(b)$_1$–(b)$_3$). Moreover, surface height distributions can offer a qualitative evaluation of the sample quality: (i) a sharp peak near 0 nm signifies minimal film roughness (following the morphology of the target substrate); (ii) peak broadening indicates the increment of both cracks and contaminations; (iii) a right (left) shift from 0 nm suggests an increase in contaminations (cracks). As displayed in figures 2(c) and (d), a sharp peak close to 0 nm suggests the advantage of our method, which becomes superior with the layer number increases. The uniformity of our stack over a large area was further confirmed by the Raman mappings based on the intensity and peak position of the A$_{1g}$ mode (figures 2(e) and (S2)). Moreover,

Figure 3. Centimetre-scale multilayer MoS_2 stacks prepared by the multiple-conformal-contact method. (a) Photograph of the as-fabricated 1, 3, 5 and 8L MoS_2 stacks on sapphire substrates using the hybrid stamps. (b) Raman spectra of the multilayer MoS_2 collected from the samples in (a). (c) The Raman peak positions and wavenumber difference $\Delta\omega$ (frequency difference between E_{2g} and A_{1g} peaks) plotted as a function of layer number. (d) Absorbance spectra of the large-area 1, 3, 5, and 8L MoS_2 stacks on sapphire substrates. (e) The cross-sectional STEM image of an as-fabricated 8L-MoS_2 sample.

the clear moiré patterns in the scanning transmission electron microscopic (STEM) images indicated the high-quality interface of the bilayer MoS_2 (figure S3). Our multiple conformal-contact transfer method can feasibly address roughness mismatches as high as 42.0 nm during transfer (figure S4), demonstrating its capability to fabricate large-area 2D stacks with high uniformity and structural integrity.

2.3. Construction of multi-layer stacks with intrinsic interfaces

To test whether the interfaces can maintain their intrinsic uniformity after multiple transfer processes, MoS_2 stacks of 3, 5, and 8 layers were fabricated using the hybrid stamp and subsequently transferred onto sapphire substrates (figure 3(a)). As shown in the Raman spectra, the E_{2g} and A_{1g} mode exhibits a red and blue shift (figure 3(b)), respectively. It results in an increment in the wavenumber difference ($\Delta\omega$) between the two modes (figure 3(c)), which is consistent with the transitions from the directly-grown monolayers to multilayers [25, 26] and the exfoliated MoS_2 flakes (figure S5), indicating clean interfaces and strong interfacial coupling between different layers. Moreover, cracks and defects are rarely observed at the surface of the 8L-MoS_2 stack, further confirming the advantage of our transfer method in maintaining the intrinsic interface quality (figure S6).
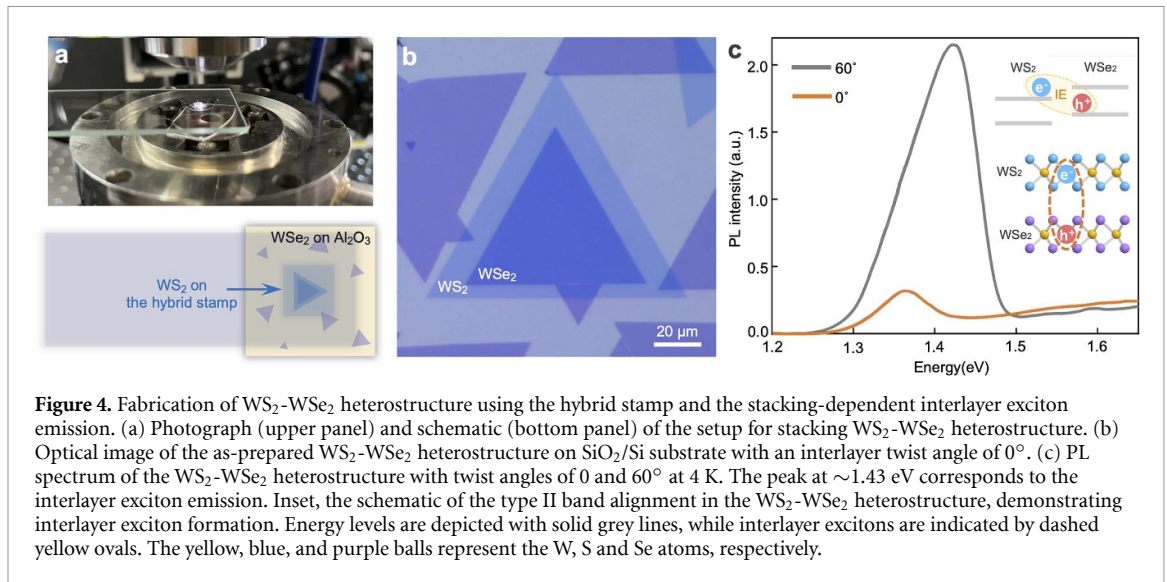
Absorption spectroscopy is a typical indication to characterize the interfaces of TMD stack, since its A and B exciton peaks are sensitive to the interface quality. As the layer number increases, the A exciton peak showed a red shift due to the decrease in the indirect bandgap, while the B exciton peak remains consistent due to a corresponding increase in the valence band splitting (figure 3(d)) [27, 28]. These exciton-related phenomena only exist when strong interfacial coupling is guaranteed, which is attributed to the intrinsic interfaces in the stack. STEM was further employed to intuitively visualize the interface at atomic scale. As displayed in figure 3(e), the intact and clean 8L-MoS_2 presents a layer spacing of $\sim$6.5 Å—the typical interlayer spacing of directly-grown MoS_2 [29].

2.4. Capability for twist angle control

Our multiple conformal-contact transfer method also enables precise control of the interlayer twist angle by integrating with a rotary transfer stage (rotation resolution of 0.1°) (figure 4(a)). A WS_2-WSe_2 heterostructure with a designed interlayer twist angle of 0° (AA stacking) was fabricated, as shown in figure 4(b). It is worth noting that, folds or cracks that frequently occurred on the edges of individual domains can be largely avoided through our method.

The WS_2-WSe_2 heterostructure exhibits a type II band alignment, wherein electrons and holes are localized in the WS_2 and WSe_2 layers under illumination, respectively (figure 4(c) inset). This spatially indirect interlayer excitons are sensitive to the interface coupling strength between two layers [30, 31]. As shown in figure 4(c), the low-temperature Photoluminescence (PL) spectra display new emission peaks at around 1.43 eV (twist angle of 60°) and 1.37 eV (twist angles of 0°) with a large intensity difference between them (the intensity at twist angle of

Figure 4. Fabrication of WS$_2$-WSe$_2$ heterostructure using the hybrid stamp and the stacking-dependent interlayer exciton emission. (a) Photograph (upper panel) and schematic (bottom panel) of the setup for stacking WS$_2$-WSe$_2$ heterostructure. (b) Optical image of the as-prepared WS$_2$-WSe$_2$ heterostructure on SiO$_2$/Si substrate with an interlayer twist angle of 0°. (c) PL spectrum of the WS$_2$-WSe$_2$ heterostructure with twist angles of 0 and 60° at 4 K. The peak at ~1.43 eV corresponds to the interlayer exciton emission. Inset, the schematic of the type II band alignment in the WS$_2$-WSe$_2$ heterostructure, demonstrating interlayer exciton formation. Energy levels are depicted with solid grey lines, while interlayer excitons are indicated by dashed yellow ovals. The yellow, blue, and purple balls represent the W, S and Se atoms, respectively.

60° is ~8 times that of 0°). The observation of such markedly different features is attributed to the precise control on twist angles. Otherwise, even minor deviations from 0° and 60° can significantly diminish the emission peaks [32–34], thereby reducing the discernibility between the two peaks. It showcases the potential of this transfer method for exploring large-area interlayer excitonic effects and corresponding applications, such as excitonic transistors, lasing, and mid-infrared photodetection [35–37].

3. Conclusion

In summary, we have developed a multiple conformal-contact transfer strategy employing a deformable hybrid stamp to fabricate TMD stacks. This method effectively prevents the introduction of defects such as cracks and impurities, and facilitates the easy transfer of stacks to target substrates with considerable roughness. Both continuous multilayer TMD stacks and TMD domain with precisely controlled interlayer twist angles are feasibly obtained, demonstrating the time efficiency of this method. Moreover, we believe that interface quality can be further improved by establishing a high vacuum environment to reduce residual air contaminants. Additionally, we propose that our transfer strategy can be adapted for the stacking of other 2D materials, thereby offering technical support for future device applications in twistronics and moiré photonics.

4. Methods

4.1. Growth of MoS$_2$, WS$_2$ and WSe$_2$ monolayers
A fused silica chip was spin-coated with an aqueous solution of Na$_2$MoO$_4$ or Na$_2$WO$_4$ with optimized concentration (Na$_2$MoO$_4$ of 12 mg·ml^{-1} for MoS$_2$ growth, Na$_2$WO$_4$ of 20 and 30 mg·ml^{-1} for WS$_2$ and WSe$_2$ growth, respectively), followed by heating at 80°C for drying. The precursor-coated fused silica, target substrate, and chalcogenide crystal plate (ZnS and ZnSe) were stacked in a sandwich manner using mica as spacers. Then the system was placed on a quartz plate and loaded into a chemical vapour deposition (CVD) furnace. The chamber was flushed with argon (100 sccm) and heated to the optimized growth temperature (~780°C, ~930°C, and 820°C for MoS$_2$, WS$_2$, and WSe$_2$, respectively). During the growth process, the system pressure was kept at ~120 Pa and the growth duration was set as 40 min. After growth, the system was naturally cooled down to room temperature.

4.2. Construction of the hybrid stamp
First, a high-concentration solution of PPC in anisole was dropped onto a sapphire substrate and dried at 50°C for 2 h (~100 mg PPC polymer could guarantee the perfect fabrication of more than 8 layers of ~1 cm^2 MoS$_2$ stacks). Subsequently, the substrate was annealed in a CVD furnace under low pressure at 160°C for 1 h to form a thick PPC buffer getting rid of anisole residual. The sapphire-supported PPC buffer was then pressed onto a PMMA-coated MoS$_2$ on SiO$_2$/Si and heated to 150°C, allowing the PPC to become fluid and fully cover the PMMA. The assembly was then cooled to 30°C, and the sapphire/PPC/PMMA/MoS$_2$ was exfoliated from the SiO$_2$/Si substrate, creating the hybrid stamp with an initial MoS$_2$ layer attached.

4.3. Fabrication and transfer of MoS$_2$ stacks with hybrid stamp
Stacking MoS$_2$ with the hybrid stamp followed periodical procedures: (i) The hybrid stamp with an initial MoS$_2$ layer attached, was pressed to laminate onto a MoS$_2$/SiO$_2$/Si and kept at 90°C for 1 min. (ii) The assembly was cooled to 30°C and then delaminated from the SiO$_2$/Si substrate by direct exfoliation. (iii) These steps are repeated until the desired number of MoS$_2$ layers are accumulated on the hybrid stamp.

The stacked MoS_2 can then be transferred to various substrates using a process similar to the lamination step of the stacking procedure. The polymer layers were removed by immersing in acetone for 3 h and annealing in a CVD furnace at 400°C for 6 h, with Ar at a flow rate of 100 sccm.

4.4. Fabrication of WS_2-WSe_2 heterostructure with designed twist angle

A home-made 2D materials transfer stage was utilized to realize the twist angle control of the WS_2-WSe_2 heterostructure. The instrument features a rotational resolution of 0.1° and an in-plane displacement resolution of 0.5 μm. The specific operation steps are as follows: (i) The selected WS_2 domain is transferred onto the hybrid stamp using the same procedure mentioned above. (ii) The hybrid stamp with WS_2 is attached to a glass slide and aligned parallel to WSe_2 domains grown on sapphire substrates using an optical microscope. (iii) Rotate the bottom WSe_2/sapphire via the stage to a form desired angle between the WS_2 and WSe_2. Then drop the top WS_2 to attach with the WSe_2. (iv) The assembly was heated to 90°C for 1 min, followed by cooling down to 30°C. The WS_2-WSe_2 heterostructure was delaminated from the sapphire substrate with water assistance and released onto a SiO_2/Si substrate.

4.5. Transfer of 2L-MoS_2 with TRT/PMMA

First, a PMMA layer was spin-coated onto the MoS_2/sapphire at 1500 rpm for 1 min, followed by drying in air at 120°C for 5 min. Then a TRT was attached to the PMMA/MoS_2/sapphire assembly. This TRT/PMMA/MoS_2 composite was then delaminated from the sapphire with water assistance and laminated onto a MoS_2/SiO_2/Si. The assembly was then kept at 120°C for 10 min to enhance the interaction between the MoS_2 layers before the TRT/PMMA/2L-MoS_2 is exfoliated and laminated onto the SiO_2/Si substrate. The TRT was removed by heating to a designated release temperature of 150°C and then peeled off, and the PMMA was removed through the same acetone-washing and annealing steps mentioned above.

4.6. Transfer of 2L-MoS_2 with PDMS

First, a PDMS layer is attached to the MoS_2/sapphire. This PDMS/MoS_2 composite is then detached from the sapphire with water assistance and attached to another MoS_2/sapphire. The PDMS/2L-MoS_2 assembly was delaminated using water assistance again and attached to a SiO_2/Si substrate. The assembly was heated at 120°C for 10 min to enhance the interaction between the MoS_2 and the substrate while reducing the PDMS adhesion. Then the PDMS was exfoliated and the 2L-MoS_2 stack on the SiO_2/Si substrate is annealed under the previously mentioned parameters to minimize PDMS residues.

4.7. Characterizations

Optical images were captured using an Olympus BX51M microscope. Raman spectra and mappings were performed with a WITec alpha300R system, employing a 514 nm laser excitation wavelength and a power of ∼5 mW. PL spectra were obtained using a Cryostation low-temperature spectral measurement system, featuring a laser excitation wavelength of 633 nm and a power of 60 μW. Absorption spectra were measured by the NKT-supercontinuum white light measurement system, utilizing a laser excitation wavelength of 540–775 nm and a power of 1.25 mW. STEM experiments were conducted using a FEI Titan Themis G2 300 operated at 300 kV. AFM images were acquired with an Asylum Research Cypher AFM system.

Data availability statement

All data that support the findings of this study are included within the article (and any supplementary files).

Acknowledgment

ORCID iDs

Yu Fu ⑩ https://orcid.org/0009-0009-2165-1404
Yilin Niu ⑩ https://orcid.org/0009-0002-6032-291X
Guodong Xue ⑩ https://orcid.org/0009-0006-4366-2401
Chang Liu ⑩ https://orcid.org/0000-0002-6273-6465
Can Liu ⑩ https://orcid.org/0000-0001-5451-4144
Kaihui Liu ⑩ https://orcid.org/0000-0002-8781-2495

References

[1] Duong D L, Yun S J and Lee Y H 2017 Van der waals layered materials: opportunities and challenges *ACS Nano* **11** 11803–30
[2] Jauregui L A *et al* 2019 Electrical control of interlayer exciton dynamics in atomically thin heterostructures *Science* **366** 870–5
[3] Sierra J F, Fabian J, Kawakami R K, Roche S and Valenzuela S O 2021 Van der Waals heterostructures for spintronics and opto-spintronics *Nat. Nanotechnol.* **16** 856–68
[4] Ye Z, Cao T, O'Brien K, Zhu H, Yin X, Wang Y, Louie S G and Zhang X 2014 Probing excitonic dark states in single-layer tungsten disulphide *Nature* **513** 214–8

[5] Wang J *et al* 2022 Dual-coupling-guided epitaxial growth of wafer-scale single-crystal WS$_2$ monolayer on vicinal a-plane sapphire *Nat. Nanotechnol.* **17** 33–38

[6] Wang Q *et al* 2020 Wafer-scale highly oriented monolayer MoS$_2$ with large domain sizes *Nano Lett.* **20** 7193–9

[7] Xia Y *et al* 2023 12-inch growth of uniform MoS$_2$ monolayer for integrated circuit manufacture *Nat. Mater.* **22** 1324–31

[8] Xu X *et al* 2021 Seeded 2D epitaxy of large-area single-crystal films of the van der Waals semiconductor 2H MoTe$_2$ *Science* **372** 195–200

[9] Xue G *et al* 2023 Modularized batch production of 12-inch transition metal dichalcogenides by local element supply *Sci. Bull.* **68** 1514–21

[10] Zuo Y *et al* 2022 Robust growth of two-dimensional metal dichalcogenides and their alloys by active chalcogen monomer supply *Nat. Commun.* **13** 1007

[11] Jung Y *et al* 2019 Transferred via contacts as a platform for ideal two-dimensional transistors *Nat. Electron.* **2** 187–94

[12] Wang Y, Kim J C, Wu R J, Martinez J, Song X, Yang J, Zhao F, Mkhoyan A, Jeong H Y and Chhowalla M 2019 Van der Waals contacts between three-dimensional metals and two-dimensional semiconductors *Nature* **568** 70–74

[13] Huang J K *et al* 2022 High-κ perovskite membranes as insulators for two-dimensional transistors *Nature* **605** 262–7

[14] Kim J Y, Ju X, Ang K W and Chi D 2023 Van der Waals layer transfer of 2D materials for monolithic 3D electronic system integration: review and outlook *ACS Nano* **17** 1831–44

[15] Mannix A J *et al* 2022 Robotic four-dimensional pixel assembly of van der Waals solids *Nat. Nanotechnol.* **17** 361–6

[16] Kumar P *et al* 2022 Light–matter coupling in large-area van der Waals superlattices *Nat. Nanotechnol.* **17** 182–9

[17] Yu Y *et al* 2015 Equally efficient interlayer exciton relaxation and improved absorption in epitaxial and nonepitaxial MoS$_2$/WS$_2$ heterostructures *Nano Lett.* **15** 486–91

[18] Shen YC *et al* 2021 Rational design on wrinkle-less transfer of transition metal dichalcogenide monolayer by adjustable wettability-sssisted transfer method *Adv. Funct. Mater.* **31** 2104978

[19] Yu H *et al* 2017 Wafer-scale growth and transfer of highly-oriented monolayer MoS$_2$ continuous films *ACS Nano* **11** 12001–7

[20] Zhu L *et al* 2022 Scalable and versatile transfer of sensitive two-dimensional materials *Nano Lett.* **22** 2342–9

[21] Kang K, Lee K H, Han Y, Gao H, Xie S, Muller D A and Park J 2017 Layer-by-layer assembly of two-dimensional materials into wafer-scale heterostructures *Nature* **550** 229–33

[22] Quellmalz A *et al* 2021 Large-area integration of two-dimensional materials and their heterostructures by wafer bonding *Nat. Commun.* **12** 917

[23] Zhao Y *et al* 2022 Large-area transfer of two-dimensional materials free of cracks, contamination and wrinkles via controllable conformal contact *Nat. Commun.* **13** 4409

[24] Hu Z *et al* 2023 Rapid and scalable transfer of large-area graphene wafers *Adv. Mater.* **35** 2300621

[25] Li H, Zhang Q, Yap C C R, Tay B K, Edwin T H T, Olivier A and Baillargeat D 2012 From bulk to monolayer MoS$_2$: evolution of Raman scattering *Adv. Funct. Mater.* **22** 1385–90

[26] Liu H L, Guo H, Yang T, Zhang Z, Kumamoto Y, Shen C C, Hsu Y T, L i LJ, Saito R and Kawata S 2015 Anomalous lattice vibrations of monolayer MoS$_2$ probed by ultraviolet Raman scattering *Phys. Chem. Chem. Phys.* **17** 14561–8

[27] Dhakal K P, Duong D L, Lee J, Nam H, Kim M, Kan M, Lee Y H and Kim J 2014 Confocal absorption spectral imaging of MoS$_2$: optical transitions depending on the atomic thickness of intrinsic and chemically doped MoS$_2$ *Nanoscale* **6** 13028–35

[28] Splendiani A, Sun L, Zhang Y, Li T, Kim J, Chim C Y, Galli G and Wang F 2010 Emerging photoluminescence in monolayer MoS$_2$ *Nano Lett.* **10** 1271–5

[29] Jeon J, Jang S K, Jeon S M, Yoo G, Jang Y H, Park J H and Lee S 2015 Layer-controlled CVD growth of large-area two-dimensional MoS$_2$ films *Nanoscale* **7** 1688–95

[30] Kang J, Tongay S, Zhou J, Li J and Wu J 2013 Band offsets and heterostructures of two-dimensional semiconductors *Appl. Phys. Lett.* **102** 012111

[31] Zheng B *et al* 2018 Band alignment engineering in two-dimensional lateral heterostructures *J. Am. Chem. Soc.* **140** 11193–7

[32] Jin C *et al* 2019 Observation of moiré excitons in WSe$_2$/WS$_2$ heterostructure superlattices *Nature* **567** 76–80

[33] Wu K, Yang Z, Shi Y, Wang Y, Xiang B, Zhou H, Chen W, Zhang S, Xu H and Xiong Q 2024 Revealing the optical transition properties of interlayer excitons in defective WS$_2$/WSe$_2$ heterobilayers *Nano Lett.* **24** 8671–8

[34] Yuan L, Zheng B, Kunstmann J, Brumme T, Kuc A B, Ma C, Deng S, Blach D, Pan A and Huang L 2020 Twist-angle-dependent interlayer exciton diffusion in WS$_2$–WSe$_2$ heterobilayers *Nat. Mater.* **19** 617–23

[35] Lukman S *et al* 2020 High oscillator strength interlayer excitons in two-dimensional heterostructures for mid-infrared photodetection *Nat. Nanotechnol.* **15** 675–82

[36] Paik E Y, Zhang L, Burg G W, Gogna R, Tutuc E and Deng H 2019 Interlayer exciton laser of extended spatial coherence in atomically thin heterostructures *Nature* **576** 80–84

[37] Unuchek D, Ciarrocchi A, Avsar A, Watanabe K, Taniguchi T and Kis A 2018 Room-temperature electrical control of exciton flux in a van der Waals heterostructure *Nature* **560** 340–4